

Chair of Optoelectronics
Institute of Computer Engineering
Heidelberg University

Annual Report 2013

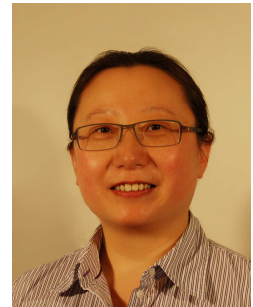
CONTENTS

| | |
|----------------------------|-----|
| Staff | II |
| Foreword | III |
| Research Projects | IV |
| Publications in 2013 | 12 |
| Imprint..... | 13 |

STAFF



Maximilian Auer
Wissenschaftlicher Mitarbeiter



Dr. Xiyuan Liu
Wissenschaftliche Mitarbeiterin



Tim Stenau
Wissenschaftlicher Mitarbeiter



Prof. Dr. Karl-Heinz Brenner
Lehrstuhlinhaber



Wolfgang Stumpfs
Technischer Angestellter



Sabine Volk
Lehrstuhlsekretärin



Torsten Paul
Student



André Junker
Student



FOREWORD

Dear reader,

This annual report describes the research activities of the chair of optoelectronics for the year 2013. This year, two main research directions emerged. One activity centers around the diffractive micro lenses in contributions on page 4, 5, 9, 11 resulting in the construction of a highly parallel wide field scanning microscope providing a 20 Megapixel image. The second, new research direction looks at effects arising from localized illumination. To this end, two new simulation methods were developed for unstructured (page 6) and for structured (page 7) layers of optical materials. Existing simulation methods generally assume an infinitely extended plane wave as light source. The new methods come along with a new model for describing the input polarization and may be useful in many application areas such as projection lithography and structured illumination microscopy.

We hope that many of the topics in this report will find your interest.

Karl-Heinz Brenner
Head of the chair

RESEARCH PROJECTS

| | |
|---|----|
| Construction of a Plenoptic Camera <i>A. Junker, T. Stenau, K.-H. Brenner</i> | 1 |
| Wave-optical Reconstruction of Plenoptic Camera Images <i>A. Junker, T. Stenau, K.-H. Brenner</i> | 2 |
| Experimental setup for the measurement of resonant effects in high-contrast gratings <i>M. Auer, K.-H. Brenner</i> | 3 |
| Phase retrieval using a diffractive micro lens array <i>X. Liu, K.-H. Brenner</i> | 4 |
| Experimental realisation and first results of a scanning microscope with a diffractive microlens array <i>T. Stenau,, K.-H. Brenner</i> | 5 |
| Localized light sources in the exact optical simulation of multilayer stacks <i>K.-H. Brenner</i> | 6 |
| Simulation of diffraction in three-dimensional optical gratings with a localized incident wave <i>M. Auer, K.-H. Brenner</i> | 7 |
| Approximations of Rayleigh-Sommerfeld Diffraction <i>K.-H. Brenner</i> | 8 |
| Accuracy of Fitting an array of spots to a model (GRIDFIT) <i>K.-H. Brenner</i> | 9 |
| Fabrication and optimization of refractive microstructures <i>T. Paul, K.-H. Brenner</i> | 10 |
| Influence of deviations from design parameters for diffractive microlens arrays <i>T. Stenau, K.-H. Brenner</i> | 11 |

Construction of a Plenoptic Camera

A. Junker, T. Stenau, K.-H. Brenner

A plenoptic camera consists of a micro lens array (MLA), which is positioned in the image plane of a classic imaging system. The image sensor is located one micro lens focal length behind the MLA (Fig. 1).

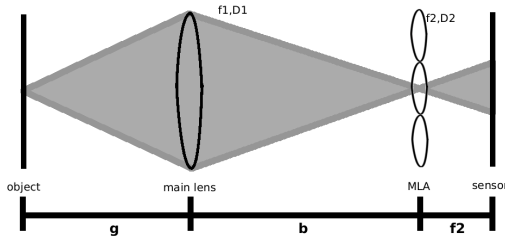


Fig. 1: Illustration of the light field camera setup.

The MLA pitch is usually chosen such that one micro lens covers approximately 10-20 sensor pixels in one dimension. Furthermore, the camera sensor ideally has a high resolution [1]. Moreover, an objective lens with small focal length and small sensor pixels are advantageous for a later wave-optical simulation / reconstruction [2].

Our setup uses an AVT Guppy F-503 industrial camera with a 5 megapixel CMOS sensor and 2.2 μ m pixel pitch. A MLA (circular lenses on a quadratic grid) with 110 μ m pitch and 0.03 numerical aperture manufactured by Süss MicroOptics is employed. We use a Tamron 25mm C-mount objective lens with adjustable aperture size. This is necessary to ensure that individual micro lens images do not overlap [1].

The housing of the Guppy camera is removed in order to access the image sensor directly. The bolts connecting the circuit boards are replaced by M2 threaded bars for the attachment of the MLA socket (Fig. 2). Four nuts (two on each threaded bar) are used to control the distance and tilt with respect to the image sensor; additionally, a spring and another screw are used to adjust the tilt in the other direction.

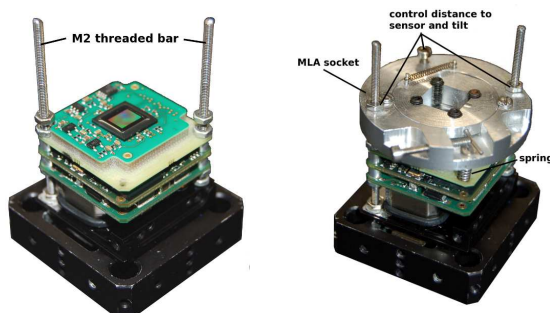


Fig. 2: Guppy camera with housing removed (left). MLA socket mounted on top of the Guppy camera guided by two threaded bars (right).

The MLA socket features a rotatable mount (Fig. 3 left), which holds the MLA inside a cavity. The lenses of the MLA point towards the objective lens. The MLA can be turned about the optical axis with an M2 screw attached to the outer socket part. The distance, tilt and rotational alignment of the MLA with the image sensor are conducted using a plane wave incident on the MLA and a subsequent analysis of the spot image with a grid fitting software [3].

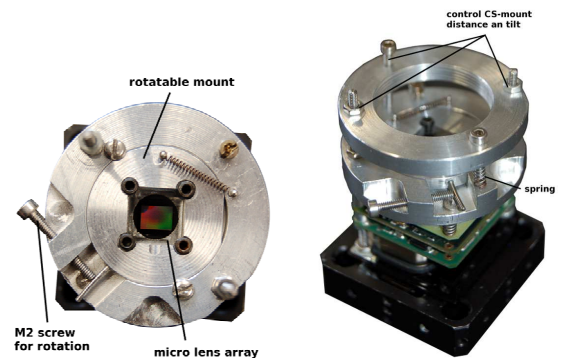


Fig. 3: MLA socket from the top view (left). Camera with C/CS-mount fitting attached (right).

The C/CS-mount fitting for the objective lens is likewise attached to the threaded bars (Fig. 3 right). The flange back distance and tilt is adjusted in the same manner as the MLA socket. A sample image of the plenoptic camera is presented in Fig. 4.

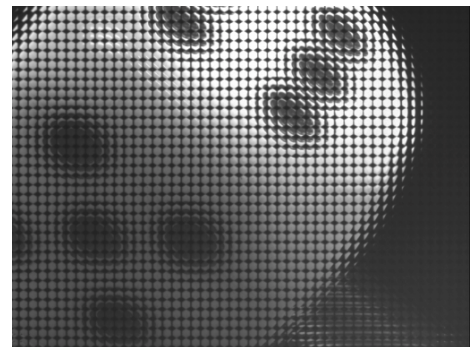


Fig. 4: Sensor image of a dice at $g=8\text{cm}$ with the objective lens focused at infinity.

References:

- [1] R. Ng, „Digital Light Field Photography” – PhD Thesis, Stanford University (2006)
- [2] A. Junker, „Wave-optical Reconstruction of Plenoptic Camera Images”, Master Thesis, University of Heidelberg (2013)
- [3] K.-H. Brenner, „Accuracy of fitting an array of spots to a model (GRIDFIT)” this report, contribution #9, University of Heidelberg (2013)

Wave-optical Reconstruction of Plenoptic Camera Images

A. Junker, T. Stenau, K.-H. Brenner

A light field camera, also called plenoptic camera, consists of a micro lens array (MLA), which is positioned in the image plane of a classic imaging system. The image sensor is located one micro lens focal length behind the MLA (Fig. 1). Such a setup is capable of capturing both positional and directional information, which results in an enhanced performance in post shot image manipulation.

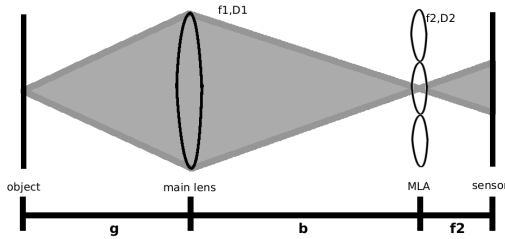


Fig. 1: Light field camera setup: $f_1, D_1 / f_2, D_2$ denote main / micro lens focal length and diameter. g and b correspond to the main lens object and image distance.

The reconstruction of light field camera images up to now has been only conducted in a ray-optical framework, as example in [1]. Since present camera sensors' pixel sizes approach the order of visible light's wavelength, it can be assumed that in combination with low aperture optical systems this approximation is not valid. Therefore, we present a scalar wave-optical object reconstruction algorithm and compare its final images to the results of a ray-optical reconstruction procedure.

Considering the field $u_0(\vec{x}_\perp)$ incident on a single micro lens, then from the image sensor data the following amplitude distribution is obtained,

$$|u_{\text{sensor}}(\vec{x}_\perp)| = \frac{1}{\lambda f_2} \left| \mathcal{F} \left[u_0(\vec{x}_\perp) \right] \left(\frac{\vec{x}_\perp}{\lambda f_2} \right) \right|. \quad (1)$$

The corresponding phase information is lost. The object reconstruction is started with a converging wave at the image sensor, which is implemented by a back-refraction through a reconstruction lens with focal length f_2 in the image sensor plane (Fig. 2). This field is then back-propagated into the MLA plane and back-refracted through the corresponding micro lens. The resulting field reads

$$u_0^{\text{recon}}(\vec{x}_\perp) = \mathcal{F}^{-1} \left[\left[\tilde{u}_0(\vec{v}) \right] \right] (\vec{x}_\perp). \quad (2)$$

This result corresponds to the true input field $u_0(\vec{x}_\perp)$, except that the object phase is lost, which originates from the measurement process at the image

sensor. The propagation phase is entirely reconstructed. From the MLA plane the field can be propagated to any desired main lens image plane. In order to introduce incoherence into the system, each micro lens image is reconstructed separately. The resulting intensity distributions are added.

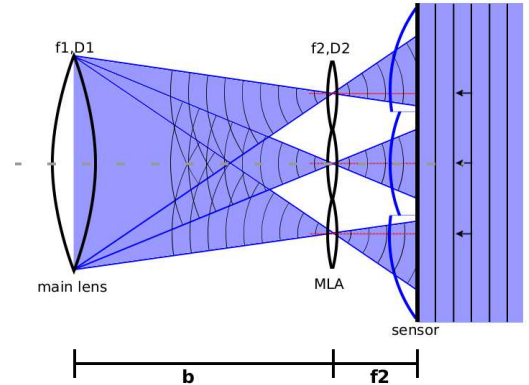


Fig. 2: Illustration of the reconstruction process. A reconstruction lens (blue) is positioned in the image sensor plane. Its optical axis (red) is aligned with the optical axis of the corresponding micro lens from the MLA. Each reconstruction lens covers the area of one micro lens image. Note that the latter are shifted relative to the micro lens centers due to the image capture process.

We implemented the Angular Spectrum algorithm for the propagation of the complex wave field. The refraction by a thin lens is realized by a multiplication with a quadratic phase factor. Fig. 3 shows the ray- and wave-optical reconstruction of a true light field image of a dice. The resolution gain is clearly visible. A more detailed analysis shows that the resolution is enhanced by an approximate factor of two [2]. Furthermore, reconstruction artifacts are suppressed more effectively.

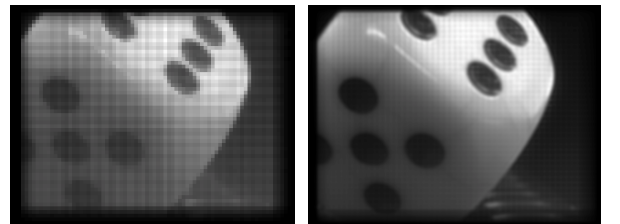


Fig. 3: Ray- (left) and wave-optical (right) reconstruction of a true light field image of a dice. We applied the algorithm presented in [1] for the ray-optical reconstruction.

References:

- [1] R. Ng, „Digital Light Field Photography” – PhD Thesis, Stanford University (2006)
- [2] A. Junker, „Wave-optical Reconstruction of Plenoptic Camera Images”, Master Thesis, University of Heidelberg (2013)

Experimental setup for the measurement of resonant effects in high-contrast gratings

M. Auer, K.-H. Brenner

For optical gratings with a feature size similar to the incident light, strong resonances can be excited, raising the degree of reflection or absorption to more than 90 %. Thus the efficiency of optoelectrical devices like detectors, solar cells or photo-lithographical systems could be improved significantly.

In order to show and study this effect not only in simulation, but in a real environment, a setup is needed that can illuminate an optical grating with a low bandwidth but sufficiently powerful beam of light. At the same time the light source needs to be angle and wavelength tunable for recording a resonance curve. A high power tungsten halogen lamp in combination with a monochromator promised to be a lower-cost alternative to a wide range tunable laser source.

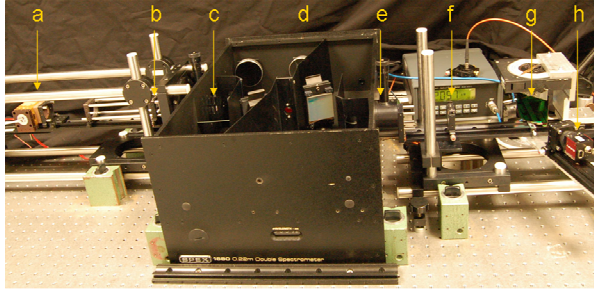


Fig. 1: Setup with tungsten halogen lamp(a), two lenses (b, f) to image the source to the entrance slit (c) of a double monochromator (d), and the exit slit (e) again to the sample grating (g). (h) is the camera.

The main challenge with this concept is to transfer a maximum amount of radiant power from the source to the detector. The limiting factors for the system throughput are the power of the light source, the etendue, the spectral width and the general system loss due to the efficiency of the optical components like lenses, mirrors and gratings.

For a Lambertian radiator, the power P of the light source is defined by the product of the etendue E and the radiance L as the latter is angle-independent. The etendue characterizes the phase space volume of an optical source. It is a function of the area A of the emitting source and the solid angle Ω , it radiates into:

$$E = \iint dA \cdot d\Omega \quad (1)$$

E is invariant when it passes a loss-less system and it is determined by the most limiting component. Keeping this in mind, the proper imaging lenses and their positions can be derived from the fixed monochromator parameters via f-number matching.

The spectral radiance L is the spectrum of radiation that is emitted from a surface into a given solid angle. The tungsten lamp, as a thermal radiator, can be

characterized approximately by a black body radiator, bandpass-filtered by the monochromator.

Comparison between Measurement and Simulation

The effective filament size A of the tungsten halogen source, derived from the black body radiation formula, was 9.66 mm^2 . With the monochromator as the limiting factor and the back reflector as an enhancer of 27.3 %, the system's etendue L was reduced to 0.022 %. In order to determine the color temperature of the source, the spectrum was measured and fitted to a black body radiation curve of 2570 K (cf. Fig 2a).

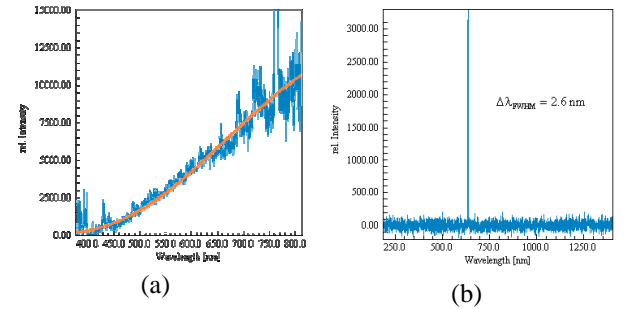


Fig. 2: a) measured spectrum of the source (blue) and black body radiation fitting curve for 2570K (orange) b) measured output spectrum of the system

The double-monochromator works in additive dispersion mode. Thus, the spectral resolution $\Delta\lambda$ depends on the slit width s and twice the linear dispersion γ of the grating:

$$\gamma = \frac{dx}{d\lambda} = f \frac{m}{P \cdot \cos(\beta_\lambda)} \Rightarrow \Delta\lambda = \frac{s}{2\gamma} \quad (2)$$

For the first diffraction order, m is one. β_λ is the corresponding diffraction angle at a wavelength of $\lambda = 636.5 \text{ nm}$. $f = 220 \text{ mm}$ is the focal length of the mirror and $P = 833.3 \text{ nm}$ is the grating period. This leads to a calculated spectral width of 2.2 nm compared to a measured width of 2.6 nm (cf Fig. 2b) and a utilization of 0.062 % of the full spectral radiance.

As a result the calculated power-throughput was $15.34 \mu\text{W}$ compared to $14 \mu\text{W}$ measured power-throughput. The remaining deviation marks the efficiency loss due to imperfect optical components. Although, the overall efficiency of the system with 90.98 W measured electrical input power seems low at such narrow bandwidth, it is still well in the range of our instrument sensibility and thus it should be useful for resonance measurements.

Phase retrieval using a diffractive micro lens array

X. Liu and K.-H. Brenner

Detectors can only record intensity, not phase. Due to this loss of phase information, indirect methods for the reconstruction of a complex wave front are still an important issue. Multi-plane phase retrieval [1,2] is a well established technique for reconstructing both, amplitude and phase of an object wave. This standard technique works best, if the intensity distribution of the object wave changes rapidly along the propagation axis. For slowly varying intensities, the iterative procedure may not converge at all. To overcome this limitation we combined the standard technique with a periodic phase element. We found that a binary diffractive phase element with overlapping aperture significantly improves the convergence of phase retrieval and thus the quality of reconstruction. Thus multi-plane phase retrieval can be applied to both rough and smooth phase distributions.

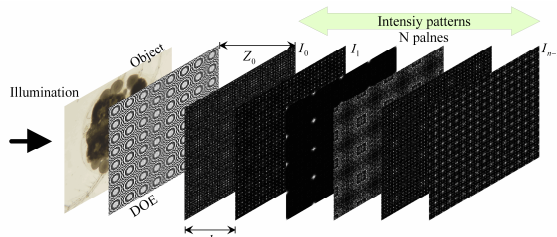


Fig. 1: Intensity recording of phase retrieval using a diffractive optical phase element

Initially we used a refractive micro lens array, which accelerated also the convergence. However, after reconstruction there is an unknown constant phase bias in each micro lens, which varies from micro lens to micro lens. The phase bias problem is due to the fact that the intensity along the optical axis of each micro lens is insensitive to a constant phase bias added to the micro lens phase. This problem can be removed completely, if the apertures of micro lens overlap. Such overlapping aperture can only be realized using diffractive optical elements.

Figure 2 shows the DOE used. The focal length f is 10 mm and the overlap factor is around 3. Detailed information about design and fabrication of such diffractive lenses can be found in [3-5]. For tolerance analysis, the parameters N , Z_0 and dz (Fig. 1) were varied in a set of numerical simulations. The reconstructions revealed that with more than 7 planes the algorithm converges quickly after 3 iterations; the distance between two adjacent planes should be larger than $f/30$. To utilize the dynamic range of the camera, the intensities should not be recorded too close to the focal plane. Therefore the initial position Z_0 should be considerably less or larger than the focal length f . Fig. 2 shows the original and reconstructed DOE.

After the DOE has been recovered, a combined phase consisting of both the object and the DOE is

reconstructed. Then the DOE phase is eliminated from the combined phase. In order to estimate the achievable accuracy of phase measurement, we used the Zernike polynomial Z_{13} as a test phase object. Fig. 3 shows the original and reconstructed phase object. The deviation is less than $\lambda/15$.

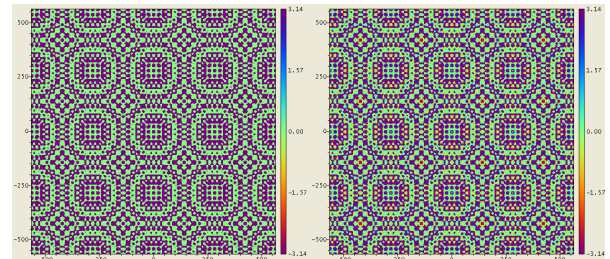


Fig. 2: Computed reconstruction of the DOE. Left: original phase; right: reconstructed phase.

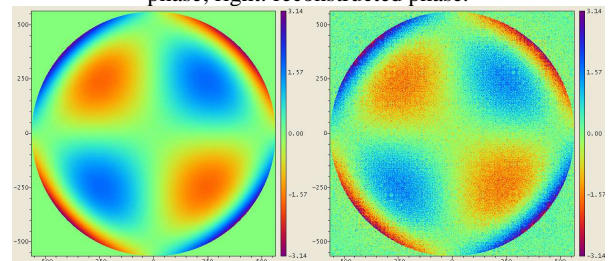


Fig. 3: Computed reconstruction of the Zernike polynomial Z_{13} as the object to be reconstructed. Left: original phase; right: reconstructed phase.

Figure 4 shows an experimental reconstruction of a dog flea; the colour image is a microscope image. The reconstruction was carried out in four iterations and the relevant parameters were: $N = 10$, $dz = 750 \mu\text{m}$ and $Z_0 = f/5$.

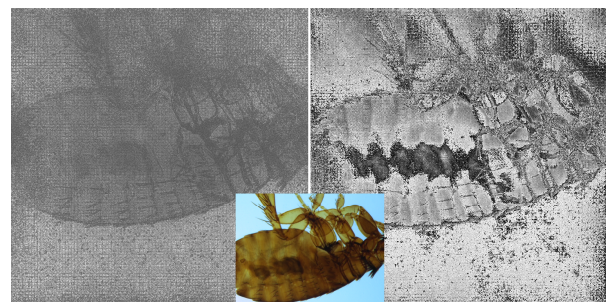


Fig. 4: Experimental reconstruction of a dog flea. Left: amplitude; right: phase; colour: microscope image.

References:

- [1] G. Pedrini, W. Osten, Y. Zhang, *OL* **30**, 833 (2005)
- [2] P. Almoro, G. Pedrini, W. Osten, *AO* **45**, 8596 (2006)
- [3] K.-H. Brenner, R. Buschlinger, *JEOS* **6**, 11204 (2011)
- [4] B. Hulsken, D. Vossen, S. Stallinga, *JEOS* **7**, 12026 (2012)
- [5] X. Liu, T. Stenau, K.-H. Brenner, 11th WIO, Quebec, Canada (2012)

Experimental realisation and first results of a scanning microscope with a diffractive microlens array

T. Stenau, K.-H. Brenner

Microscopic imaging of large samples with high spatial resolution is a challenging area of research.

Our approach uses a multi spot focal scanning technique [1]. Here, the sample is illuminated spot wise by a diffractive microlens array and the transmitted intensity is recorded. The sample is scanned by moving the microlens array. Afterwards, a high resolution image is reconstructed.

By the use of a novel overlapping diffractive microlens array [1, 2] it is possible to realise a long working distance between the microlens array and the sample and small focal spots at the same time. This is a significant contrast to conventional refractive microlens arrays. As a by-product, this enables an easier handling of the probes.

The scanning principle enables the use of an imaging optics with a relatively low numerical aperture.

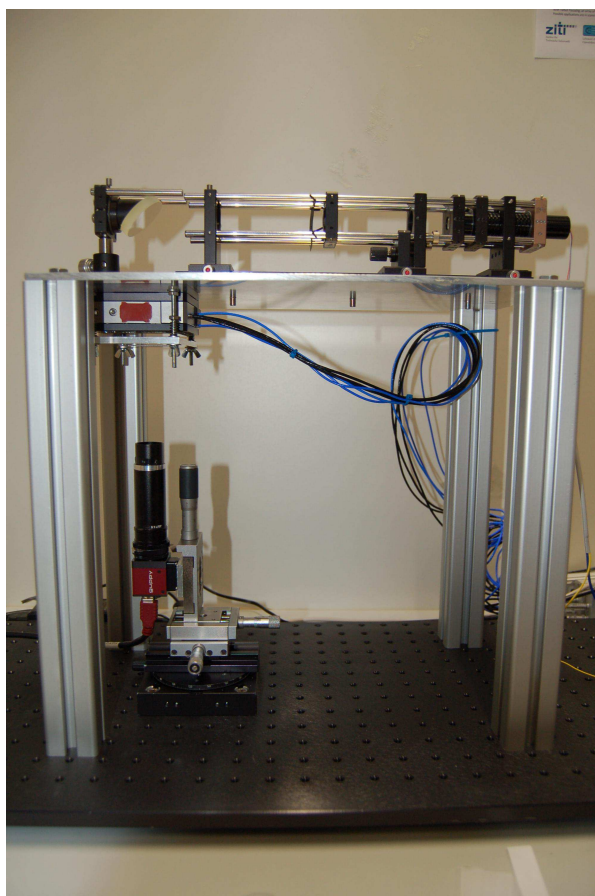


Fig. 1: Experimental setup of the microscope.

The experimental setup of the scanning microscope is shown in Fig. 1. The position of the diffractive microlens array is controlled by a piezo table with an accuracy of 20 nm. The spacing between adjacent foci is 52.8 μm , the design numerical aperture of each foci

is $\text{NA} = 0.07$ and the focal length is 3 mm. The camera uses a 1:1 imaging optic with f-number 8.

During the measurement, the array of focal spots scans the sample. This spot grid is imaged with a camera. Due to the scanning principle, each spot on the camera corresponds to one position of the sample which is responsible for the intensity loss measured with the camera.

The reconstruction algorithm first estimates the grid parameters of the focal spot grid at the first image. Then, a natural neighbour interpolation determines the intensity at the focal positions. The grid parameters for the next images are calculated by the known shift of the piezo.

Figure 2 shows a reconstruction of a green algae (Hydrodictyon Chlorophyceae) with 19Mpx. The pixel size is 1.1 μm , which is half the resolution of the camera in use.

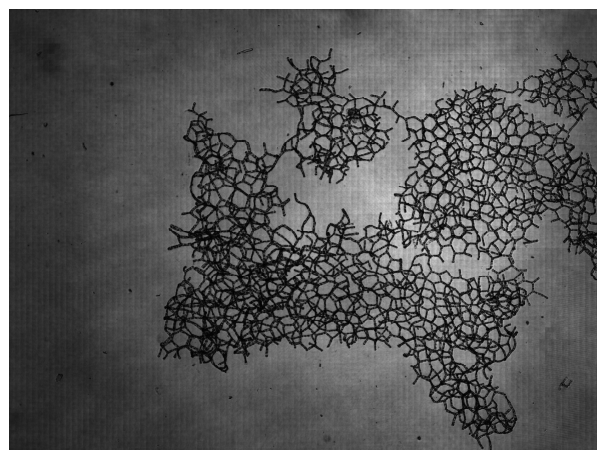


Fig. 2: Reconstruction of a green algae with twice the camera resolution.

References:

- [1] K.-H. Brenner, T. Stenau, M. Azizian „Entwicklung eines scannenden Mikroskops mit diffraktiven Mikrolinsen“, Jahrestagung der Deutschen Gesellschaft für angewandte Optik e. V. in Braunschweig (2013)
- [2] B. Hulsken, D. Vossen, S. Stallinga, “Parallel image scanning with binary phase grating”,- J. Europ. Opt. Soc. Rap. Publ. 6, 11024 (2011)

Localized light sources in the exact optical simulation of multilayer stacks

K.-H. Brenner

For the exact electromagnetic simulation of stratified layers of optical materials the multilayer matrix theory is well established [1]. This theory assumes an infinitely extended plane wave as input field. There are many situations, where an infinitely extended plane wave is not adequate for the analysis of the optical application. In optical storage as well as in confocal microscopy, the structure to be tested, is placed inside a sequence of layers and the readout light is highly focused. In optical lithography, a high resolution mask pattern is imaged into a layer of photo resist on glass. Also, in this case, the resulting light distribution cannot be modelled by an infinitely extended plane wave. Previous approaches [2,3] to treat problems of this type decompose the input field into a series of plane waves. Because the multilayer matrix theory distinguishes between TE and TM-polarization, each plane wave additionally has to be decomposed into these two polarization components.

Our approach also assumes a plane wave decomposition, but the decomposition into TE and TM-components does not provide any advantage when multiple plane wave components are considered. To this end, we have reformulated multilayer matrix theory in terms of a cartesian decomposition instead of a TE-TM decomposition. The result is a more simple set of matrix equations, which can be solved in a straight forward manner.

To use the new approach, the incident electromagnetic field also must be described by its x- and y-components. In our software, we distinguish three cases: radial polarization, azimuthal polarisation and linear polarization. It turns out that azimuthal polarization is equivalent to all modes being TE-polarized. Likewise, radial polarization is equivalent to all modes being TM-polarized. The description of linear polarization might seem to be the simplest, but in fact, the opposite is true. For a description of linear polarization, we adopted the model configuration from [2,3], but derived a new formula in a more direct way:

$$\vec{E}_i = \left(\frac{-s_y \cos \varphi + s_x \sin \varphi}{s_{\perp}^2} \right) \begin{pmatrix} -s_y \\ s_x \\ 0 \end{pmatrix} + \left(\frac{s_x \cos \varphi + s_y \sin \varphi}{s_{\perp}^2} \right) \begin{pmatrix} s_x s_z \\ s_y s_z \\ -s_{\perp}^2 \end{pmatrix} \quad (1)$$

The formula describes the incident electric field for one mode with propagation direction $\vec{s} = \vec{k} / k$,

polarized under an angle φ to the x-axis. By comparison with the results of [2,3] we found that [2] agrees exactly for pure x-polarization.

To show some examples, we first looked at focusing in air. Radial polarization is generally assumed to have superior focusing properties. We found that this assumption is only true for extremely high NAs. For NA below 0.7, the opposite is true as shown in fig. 1

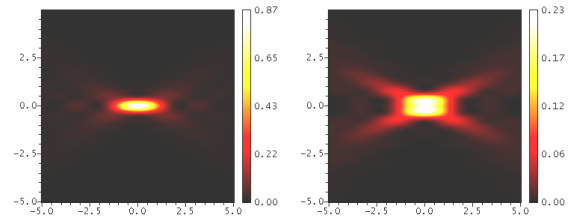


Fig. 1: Comparison $I(x, z)$ of linear (left) and radial polarization (right) for an NA of 0.5, $\lambda = 633\text{nm}$

The next example (fig.2) shows coupling of light into a stack of glass-air-glass, with $n_{\text{glass}} = 1.8$.

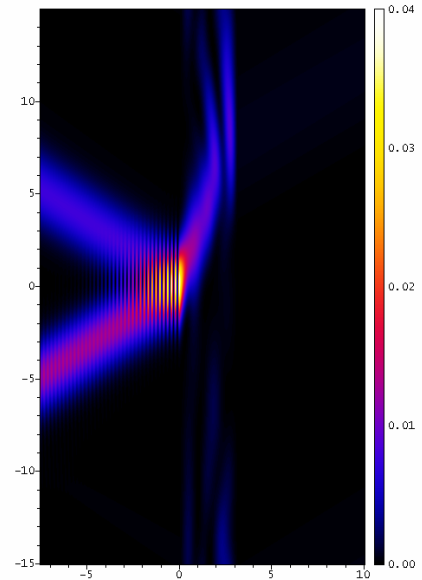


Fig. 2: Focusing a linear polarized Gaussian beam into a stack of glass-air-glass

References:

- [1] M. Born and E. Wolf. Principles of Optics. Cambridge University Press 1999, p.54.
- [2] M. Mansuripur: J. Opt. Soc. Am. A, Vol. 3 (1986) 2086.
- [3] D.G. Flagello, T. Milster, Appl. Opt. 36, (1997) 8944

Simulation of diffraction in three-dimensional optical gratings with a localized incident wave

M. Auer, K.-H. Brenner

The Rigorous Coupled Wave Analysis (RCWA) is a powerful tool for the simulation of diffraction effects in periodic structures. However, like in most other diffraction theories, the RCWA acts on the assumption, that the exciting light is a single plane wave.

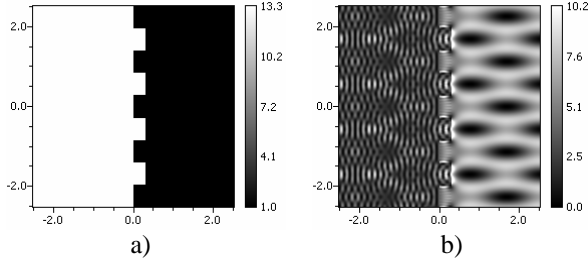


Fig. 1: a) z-x-Geometry of a diffraction grating ($P = 1.125\mu\text{m}$, $n_1=3.65$, $n_2=1$). b) Electromagnetic field excited by a plane wave illumination ($\vartheta = 0^\circ$, $\lambda=1\mu\text{m}$, TM-polarization, 120 Modes) in the same region.

In practical optical setups though, perfect plane waves are rarely available and sometimes not even favoured.

In this work, we developed a new method, which is a combination of the Plane Wave Decomposition (PWD) and a modified version of the standard RCWA algorithm. In contrast to few other approaches that have been made [1], the new method utilizes existing properties of the RCWA and thus does not require any additional calculation effort. As a Fourier Modal Method, the RCWA solves the diffraction problem in the frequency domain. Periodic space functions thereby lead to discrete Fourier-coefficients, which can be interpreted as modes or plane waves. In incoherent superposition they describe the electromagnetic fields inside and outside of an illuminated grating. Although the RCWA naturally propagates several modes in a vectorial form, the classical implementation only implies a zeroth mode for excitation. The key idea of our new approach is to use the linear nature of the RCWA to superpose multiple input signals and their responses within a single calculation. Therefore, the incident mode vector is filled with additional higher modes as a reasonable complement to the modal method concept.

In order to determine the proper mode weights of the incident wave, the PWD (eq. 1) is a suitable method as it decomposes any arbitrary wave function into its Fourier modes.

$$A_{m,n} := \frac{1}{P_x P_y} \int_0^{P_x} \int_0^{P_y} f(\mathbf{r}_\perp) e^{-2\pi i \left(\frac{m x}{P_x} + \frac{n y}{P_y} \right)} dx dy \quad (1)$$

Here, A is a vector of Fourier-coefficients with mode indices m and n for a given two-dimensional incident wave function f at $z = 0$ with periodicity P_x and P_y .

Besides the scalar amplitude, also the polarization can be defined in analogy to the standard approach, but separately for every individual mode:

$$B_{m,n}(\psi) := \frac{1}{s_\perp} \begin{pmatrix} s x_{m,n} s z_{m,n} \cdot \cos(\psi) - s y_{m,n} \cdot \sin(\psi) \\ s y_{m,n} s z_{m,n} \cdot \cos(\psi) + s x_{m,n} \cdot \sin(\psi) \end{pmatrix} \quad (2)$$

This makes it possible to implement true radial ($\psi = 0^\circ$) as well as azimuthal ($\psi = 90^\circ$) polarization and any form in between. However, linear polarisation is still possible with the new formulation (see previous article).

Thus, $L = A \cdot \Phi(\psi)$ replaces the classical incident vector, formerly described by a Kronecker delta.

Also in contrast to the standard algorithm, the new approach has neither the need nor the justification for a pseudo-periodicity, which is usually used to handle slanted incidence. Linked therewith is the necessity to define the Toeplitz-matrix, which contains the material coefficients, in a cyclic manner.

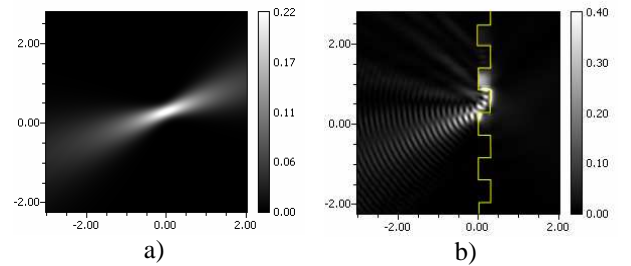


Fig. 2: a) Converging Gaussian beam ($\sigma = 0.2\mu\text{m}$, linearly polarized). b) Electromagnetic field at a grating, excited by a focussed Gaussian beam (cf. a).

As illustrated in Fig. 2 this new formulation allows grating structures that are illuminated by localized fields to be simulated and studied in a rigorous and efficient way.

The accuracy of the method depends on the spectral width of the functions defining the incident wave and the grating versus available computational resources.

References:

[1] Wu, Shun-Der, et al. "Three-dimensional converging-diverging Gaussian beam diffraction by a volume grating." *JOSA A* 22.7 (2005): 1293-1303

Approximations of Rayleigh-Sommerfeld Diffraction

K.-H. Brenner

It is interesting to see, how many different diffraction formulae were derived from the Sommerfeld Typ I diffraction integral in the literature. References [1..5] only list some representative ones. If the assumptions and the approximations in the derivation were the same, these representations should all be equal. In fact, they are not equal. In the simplest cases only the forefactor is omitted, resulting in a different amplitude. In another frequent representation [2], the Kirchhoff diffraction integral is used as a basis. For plane wave illumination, the gradient of the initial scalar field must be chosen correctly, which in the case of binary amplitude masks is almost impossible. In other examples, [3,4] the approximation of the exponential is not sufficiently accurate.

In its most general form, the Sommerfeld Type I diffraction integral can be written as:

$$u(\vec{r}) = -\frac{1}{4\pi} \iint_{S'} u(\vec{r}') \bar{\nabla} \left(\frac{e^{ik|\vec{r}'-\vec{r}|}}{|\vec{r}'-\vec{r}|} \right) d\vec{A}' \quad (1)$$

From this integral, three different specializations can be derived. In the first case (c1), the source plane S' is a spherical surface with radius f around the coordinate center. This case is used in the well known Debye integral [1]. In ref [1], however a forefactor $1/f$ is missing. In the other two cases, the source plane S' is flat and perpendicular to the z -axis. In the high NA far field diffraction case (c2), the source plane \vec{r}' is assumed to be small and the destination plane \vec{r} is assumed to be large. Case 3 (c3) is exactly the opposite and can be considered as the flat screen equivalent of the Debye integral. In this case, a focusing lens should be included in $u(\vec{r}')$ to assure that the destination plane is small.

In this report, we concentrate on case c2, the high NA far field approximation, which can be derived from eq. 1, yields

$$u(\vec{r}) = -\frac{i}{\lambda R^2} z e^{ikr} \mathcal{F} \left(u(\vec{r}'_{\perp}) e^{ik\frac{r_{\perp}^2}{2z}} \right)_{\vec{v}=\frac{1}{\lambda r}} \quad (2)$$

Interestingly, there is only one paper in the literature [5] which shows this result. The inclusion of the quadratic phase factor in eq. 2 is named the "integrated propagator" and was only added for completeness. In our analysis, we found that this factor is essential for an accurate simulation.

Example 1 shows a test pattern which was chosen to demonstrate the difference. It contains two letters F and G in a certain arrangement as binary amplitude mask. Without the integrated propagator, only a scaled version of the Fourier transform is computed. Since the Fourier intensity is shift invariant, the result is insensitive to the geometric arrangement of the letters.

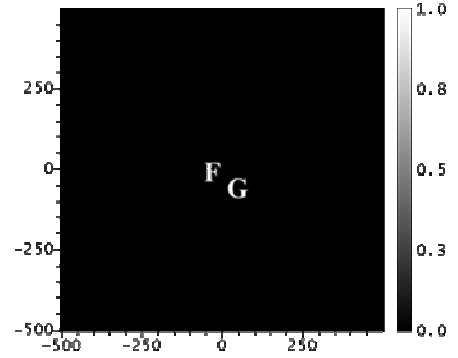


Fig. 1: Test pattern for the comparison in fig. 2. Dimensions are in μm .

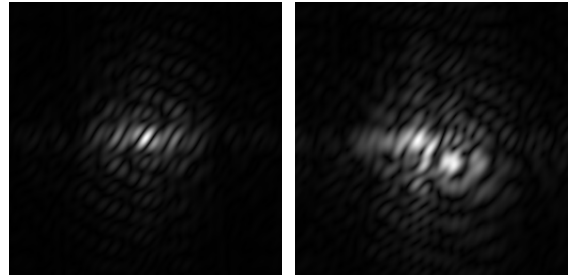


Fig. 2: Comparison of High NA diffraction over a propagation distance of 4 mm according to eq.2 without (left) and with (right) integrated propagator

A comparison with the angular spectrum method, which at this distance is still valid, shows that the integrated propagator shows the correct result.

References:

- [1] M. Born and E. Wolf. Principles of Optics. Cambridge University Press 7. edition (1999), p.485.
- [2] J. Garcia-Sucerquia, W. Xu, S. K. Jericho, P. Klages, M. H. Jericho, and H. J. Kreuzer, Appl. Opt. 45, (2006), 836.
- [3] Y. Takaki and H. Ohzu, Appl. Opt. 38, (1999) 2204
- [4] P. Bao, G. Situ, G. Pedrini, W. Osten: Appl. Opt. 51, (2012), 5486.
- [5] Y. M. Engelberg and S. Ruschin, J. Opt. Soc. Am. A 21, (2004), 2135.

Accuracy of Fitting an array of spots to a model (GRIDFIT)

K.-H. Brenner

The Shack-Hartmann wave front sensor [1] is a typical example of utilizing an array of spots in optical metrology. Another example is the light needle approach [2], which solves the problem of the normal ambiguity in reflective deflectometry. In most cases, the spot deviation can be measured by comparison with plane wave illumination, which provides reference positions for the optical axes of each micro lens. This method, however, demands high accuracy in the generation of this planar reference wave. For highest accuracy measurements, one cannot assume a perfect planar reference. The approach we have considered in this work, assumes that the spot array was created by an optical array element, which was generated with lithographic accuracy. Therefore, the grid period of the optical element is the only quantity, considered to be accurate. The mathematical model for describing the grid is defined by the 2D-vectors:

$$\vec{r}_{j,k} = j \cdot \vec{P}_1 + k \cdot \vec{P}_2 + \vec{O} \quad (1)$$

This model includes all possible linear transformations such as shift, shear and rotation. The fabricated grid element is considered to have the ideal offset $\vec{O} = 0$ and the period vectors $\vec{P}_1 = P_x \vec{e}_x$ and $\vec{P}_2 = P_y \vec{e}_y$, where P_x and P_y are the periods defined by the lithography. The task of fitting an array of measured spots to a grid is equivalent to finding 6 unknown parameters a, b, c, d, e, f defined by

$$\vec{P}_1 = \begin{pmatrix} a \\ b \end{pmatrix}, \vec{P}_2 = \begin{pmatrix} c \\ d \end{pmatrix}, \vec{O} = \begin{pmatrix} e \\ f \end{pmatrix} \quad (2)$$

and it consists of three relevant subtasks. The first task, the measurement of the center of gravity of each spot is common practice in each Shack Hartmann Sensor algorithm and is considered as known. The second task, the labeling of each spot with the pair of numbers (j, k) is a non-trivial task if the measured spot separation varies over the sensor array, or if the recorded spot array has a rotation. We solved this problem by starting with an estimated period and by dividing the measured center positions by this period and taking the fractional part. Next, we average these fractional positions. Because the fraction is a cyclic quantity, we cannot apply a simple averaging procedure. Instead we apply cyclic averaging, resulting in an averaged offset \vec{o}_{avg} , and the labels can now be found simply by

$$\begin{pmatrix} j \\ k \end{pmatrix} = \text{round} \left(\frac{\vec{r}_m - \vec{o}_{avg}}{P} \right) \quad (3)$$

where $\text{round}()$ is a round to nearest function and $P = P_x = P_y$ was assumed. Thus, we can label the measured spot centers by $\vec{p}_{j,k} = \vec{r}_m$. The final task is a least square fit, which is applied in a straight forward manner by minimizing a cost function:

$$\sum_j \sum_k (\vec{r}_{j,k} - \vec{p}_{j,k})^2 \rightarrow \min . \quad (4)$$

It provides the 6 unknowns $a .. f$. Thus the grid orientation and the period of the measured spots can be determined with high accuracy. Based on statistical analysis, the accuracy of the period scales with the inverse square root of the number of spots and is thus much higher than the single spot measurement. This accuracy is limited by the photon count and is typically in the order of $d/10 .. d/50$, where d is the pixel spacing of the detector array. With nowadays cameras and with 1000 spots, thus a period accuracy of 1 nm can be achieved. With this accuracy, spherical wave front errors can be detected with high accuracy.

For a test of the offset accuracy, we compared a measurement of an unshifted pattern with a measurement of a pattern shifted by a specified amount (fig. 1). A comparison shows an accuracy between 6 nm and 40 nm in the worst case.

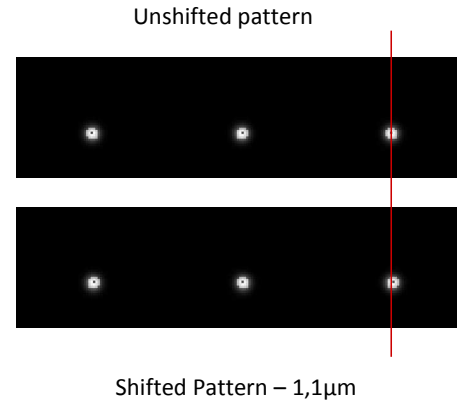


Fig. 1 Comparison of an unshifted pattern with a pattern shifted by 1.1 μm . The shift could be recovered with an accuracy of less than 40 nm.

References:

- [1] D. Malacara, Optical Shop Testing (Wiley, New York, 1991), pp. 472-484.
- [2] U. Krackhardt, J. Bähr.; Formerrfassung von reflektierenden Oberflächen in Echtzeit. Patent Offenlegungsschrift DE 10 2005 007 244.5 vom 24.08.2006.

Fabrication and optimization of refractive microstructures

T. Paul, K.-H. Brenner

The initial aim of this project was to fabricate refractive spherical and cylindrical lenses with an option to extend these to more general surface relief structures. As a fabrication method we chose thermal reflow [1] with positive photo resist. The calculation of the process and an estimate of the final form were achieved by the use of an Euler-Lagrange formalism to minimize the area surface under constant volume.

The project's experimental part covers the construction phase beginning with several test and measure structures to obtain complete knowledge of the thermal and optical properties of AZ9260, which was the photo resist in use.

The measurement phase includes determination of the spinning curve, the determination of the n and k parameters and the dynamic behavior of developed resist structures under thermal heating.

These measurements lead to a stable parameter set which allows forming structures between 6 and 15 μm thickness with an error of 0.05 μm .

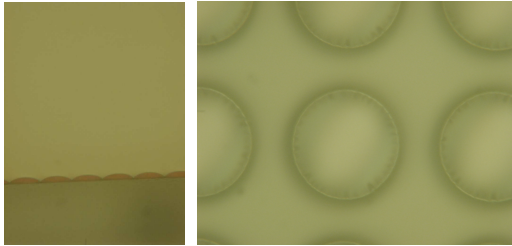


Fig. 1 Microscopic side view of cylindrical lenses and top view of spherical lenses after reflow

Parallel to these measurements it was important to optimize the form of the lens structures after thermal reflow. We describe this procedure as a minimization of the area surface A , keeping the volume V constant

$$dA = \sqrt{1 + h_x^2 + h_y^2} \cdot r \quad (1)$$

For the height function $h(x, y)$, h_x and h_y are the partial derivatives with respect to x and y . Likewise

$$dV = h(x, y) dx dy \quad (2)$$

Assuming rotational symmetry and transforming these equations to polar coordinates, we can derive the Lagrange function under volume conservation:

$$L = \left(\lambda \sqrt{1 + h_r^2} - h \right) \cdot r \quad (3)$$

Now h_r is the partial derivative with respect to the radial coordinate. The Euler-Lagrange equation then is

$$\frac{d}{dr} \frac{\partial}{\partial h_r} L - \frac{\partial}{\partial h} L = 0 \quad (4)$$

The minimization parameter λ in eq. 3 has the physical interpretation of a curvature radius. For a filled circle structure in resist, the molten cylinders result in a segment of a perfect sphere.

Due to the resist's absorption and high refractive index of 1.62 it is not favourable to use these structures directly as optical components.

Therefore silicon based PDMS was used to form a highly detailed negative copy. Tests show that even structural details below 0.5 μm were reproduced via PDMS.

In the following, we used these PDMS copies as stamps for a second reproduction.

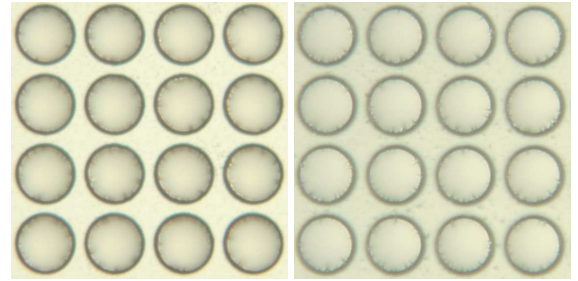


Fig. 2 Top left: Negative PDMS lenses, top right: positive AZ9260 lenses, Bottom: negative PDMS cylindrical lenses

For this reproduction step, we use UV-active polymer, which is filled into the negative PDMS structures to produce very resilient lenses with optical properties close to glass.

With this process, we want to fabricate also unconventional lenses with a thickness larger than the diameter or with non-spherical shapes.

References:

- [1] Daly, D; Stevens, R F; Hutley, M C Davies, N: "The manufacture of micro lenses by melting photo resist", Measurement Science and Technology. **1**. Bristol IOP PUBLISHING Ltd, p.759-766, (1990)

Influence of deviations from design parameters for diffractive microlens arrays

T. Stenau, K.-H. Brenner

Binary diffractive microlens arrays do not underlie the same strict relations between focal length, period and numerical aperture as refractive microlens arrays. For practical purposes, binary phase arrays with a phase height of π are used. Fabricated diffractive microlens arrays differ from the design due to production artefacts.

The focal length, the numerical aperture, the design wavelength and the period of the element are specified during the design. Then a hologram with a given pixel size is calculated.

$$u_{\text{Hologram}}(r_{\perp}) = \iint P_{NA,\lambda}(\rho_{\perp}) e^{-ik_0 f \sqrt{1-\lambda^2 \rho_{\perp}^2}} e^{2\pi i \rho_{\perp} \cdot r_{\perp}} d\rho_{\perp} \quad (1)$$

For easier fabrication, this hologram is manipulated so that the phase is quantized and the amplitude is set to one.

To evaluate the foci of this diffractive microlens array the energy in the focal ellipsoid around the design focus is measured as a figure of merit for the light concentration.

$$\left(\frac{x}{0.5 \frac{\lambda}{NA}} \right)^2 + \left(\frac{y}{0.5 \frac{\lambda}{NA}} \right)^2 + \left(\frac{z}{2 \frac{\lambda}{NA^2}} \right)^2 \leq 1 \quad (2)$$

As a first parameter we consider the influence of the deviation from the design phase height π . This deviation is directly related to a height deviation in the coating process. In Fig. 1 it can be seen that small derivations lead to small differences in the energy inside the focus.

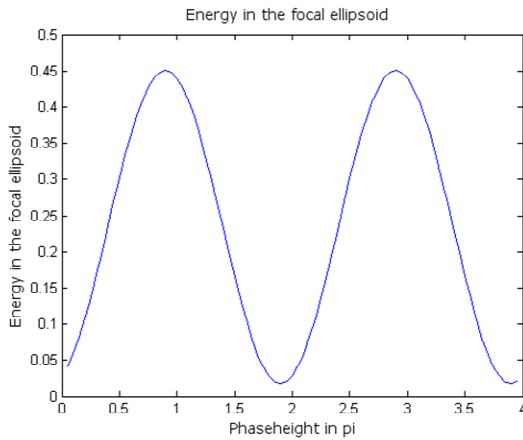


Fig. 1: Energy inside the focus ellipse as a function of the phase height of the diffractive microlens array.

Due to the focus profile of the laser lithography and the wet chemical processing, the edges of the phase structure blur. To take this into account the phase structure is convolved with a Gaussian function. The result is shown in Fig. 2. Again, the deviation from the design results in a smooth change of the energy in the ellipsoid around the focus.

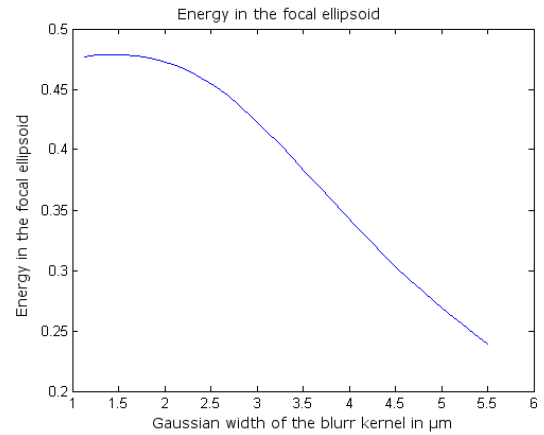


Fig. 2: Energy inside the focus ellipse as a function of the blur of the profile.

Finally, we investigate the usage of a wavelength different to the design wavelength. Figure 3 shows that the element works also for other wavelengths, only the foci are shifted.

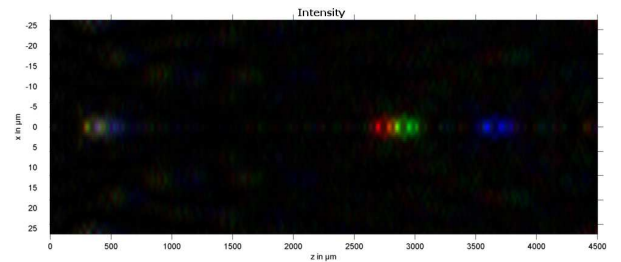


Fig. 3: Intensity profile for three different illumination wavelengths.

To conclude we observed that diffractive microlens arrays are robust against small deviation in phase height, blurring of the edges and also work at different wavelengths.

References:




- [1] T. Stenau, K.-H. Brenner, „Analyse der Designparameter von binären diffraktiven Mikrolinsenarrays in Hinblick auf den Herstellungsprozess“, Jahrestagung der Deutschen Gesellschaft für angewandte Optik e. V. in Braunschweig (2013)

PUBLICATIONS

1. K.-H. Brenner and X. Liu “Phase retrieval from multi-plane intensity measurements with wavefront sensing”, *Digital Holography and 3D Imaging*, 21.-25. April 2013, ISBN: 978-1-55752-964-0, <http://dx.doi.org/10.1364/DH.2013.DTh4A.8>, Hawaii, USA (2013)
2. T. Stenau, K.-H. Brenner, “Analyse der Designparameter von binären diffraktiven Mikrolinsenarrays in Hinblick auf den Herstellungsprozess”, (*Online-Zeitschrift der Deutschen Gesellschaft für angewandte Optik e. V.*), ISSN: 1614-8436-urn:nbn:de:0287-2013-P051-0 114. Jahrestagung, 21.-25. Mai 2013, Braunschweig, (2013)
3. X. Liu, K.-H. Brenner, “Iterative Phasenrekonstruktion mit einem diffraktiven Element”, (*Online-Zeitschrift der Deutschen Gesellschaft für angewandte Optik e. V.*), ISSN: 1614-8436-urn:nbn:de:0287-2013-B001-5 114. Jahrestagung, 21.-25. Mai 2013, Braunschweig, (2013)
4. K.-H. Brenner, T. Stenau, M. Azizian, “Entwicklung eines scannenden Mikroskops mit diffraktiven Mikrolinsen”, (*Online-Zeitschrift der Deutschen Gesellschaft für angewandte Optik e. V.*), ISSN: 1614-8436-urn:nbn:de:0287-2013-B024-6 114. Jahrestagung, 21.-25. Mai 2013, Braunschweig, (2013)
5. X. Liu, K.-H. Brenner, „High resolution wavefront measurement with phase retrieval using a diffractive overlapping micro lens array“, *7th International Workshop on Advanced Optical Imaging & Metrology (Fringe 2013)*, Springer Verlag, DOI: 10.1007/978-3-642-36359-7_35, ISBN 978-3-642-36358-0, ed. W. Osten, pp 233-236, 08.-11.09.2013, Nürtingen, (2013)
6. A. Junker, Tim Stenau, K.-H. Brenner, „Wave optical reconstruction of plenoptic camera images“, *7th International Workshop on Advanced Optical Imaging & Metrology (Fringe 2013)*, Springer Verlag, DOI: 10.1007/978-3-642-36359-7_14, ISBN 978-3-642-36358-0, ed. W. Osten, pp 117-122, 08.-11.09.2013, Nürtingen, (2013)

IMPRINT

Publisher: Prof. Dr. Karl-Heinz Brenner
Chair for Optoelectronics
Institute of Computer Engineering (ZITI)
Heidelberg University
B6, 23-29, Bauteil C
68131 Mannheim
GERMANY

 +49 (0) 621 181 2700
 +49 (0) 621 181 2695
 <http://oe.ziti.uni-heidelberg.de>

Layout: K.-H. Brenner, S. Volk

Type of publication: Online

Publication date: 2014

For quotation of any of these contributions, please use:

Reference: Annual Report 2013
Chair of Optoelectronics,
Heidelberg University
ISSN 2197 - 4462